

Experimental and numerical study on the interaction of a water mist spray with a turbulent buoyant flame

Shogo Noda^{a,b}, Bart Merci^b, Futoshi Tanaka^c, Tarek Beji^{b*}

^aMechanical Engineering, Graduate School of Engineering, University of Fukui
3-9-1 Bunkyo, Fukui-shi, Fukui 910-8507, Japan

^bGhent University, Department of Structural Engineering and Building Materials, Sint-Pietersnieuwstraat 41, B-9000, Ghent, Belgium

^cMechanical Engineering, Faculty of Engineering, University of Fukui
3-9-1 Bunkyo, Fukui-shi, Fukui 910-8507, Japan

* Corresponding author's email: Tarek.Beji@UGent.be

Highlights:

- A gas analysis system is used to accurately characterize the heat balance
- The cooling power of the spray is estimated using a single temperature measurement
- The water spray is well characterized experimentally and numerically
- The cooling power of the spray is underpredicted by about 34 %
- The reduction in the radiative heat flux to the surroundings has not been predicted

Abstract:

This paper presents a detailed experimental and numerical study on the interaction, at a reduced scale, between a turbulent buoyant propane flame of about 15.5 kW and a water mist spray with a flow rate of 0.43 L/min from a nozzle positioned at 1 m above the burner. The water spray has been characterized experimentally without a fire, by measuring the water mass flux and droplet size distributions at the level of the burner surface. The whole assembly was installed under a hood and the following three parameters were measured: (1) the chemical heat release rate (HRR) (using the oxygen consumption method), (2) the rise in gas temperature at the top, and (3) the radiative heat flux at 0.72 m from the axis of the burner and at a height of 0.05 m. Reductions of about 40% and 30% were recorded for, respectively, the gas temperature (in the hood) and the radiative heat flux, while the chemical HRR did not change. Computational Fluid Dynamics (CFD) simulations with the Fire Dynamics Simulator (FDS, version 6.7.0) predicted relatively well the gas temperature, without a reduction in the HRR, but, in contrast to the experiments, the radiative heat flux did not change.

Keywords: water mist; turbulent buoyant flame; experiments; CFD

1. Introduction

Water mist sprays are widely used in the suppression and control of fires. It is well-known that water mist spray systems can: (1) suffocate the fire (reduced oxygen supply), (2) block thermal radiation, and (3) cool smoke. A specific configuration in this regard is when the water spray is

positioned directly above the heat source, as is the case in the present study. It is important to first characterize the water mist spray pattern, given the variety of patterns that could be generated using the same spray nozzle. For example, in [1] and [2], water sprays from a single nozzle and a multi-nozzle set-up were characterized in terms of droplet diameter distribution, water flux, and droplet velocities.

The interaction between a water mist spray and several types of heat source, such as hot air jet, liquid fuel fires, gas fuel fires, and wood-crib fires, has been studied in [3–5]. In [3], velocity fields of the ceiling layer were measured. Under the effect of the water spray, the peak velocity in the ceiling jet was reduced by 50% and the layer thickness increased by a factor of 4. In [4] and [5], the suppression and extinguishment of liquid and wood-crib fires were studied for different water mist spray conditions.

However, such experiments are very costly. Therefore, Computational Fluid Dynamics (CFD) simulations are a very useful ‘support’ tool in this context. In [6] and [7], e.g., the influence of a water mist spray on the ceiling-jet underneath a horizontal ceiling plate, created by a vertical upward jet of hot air, was reproduced very well. In [8], it has been reported that the heat release rate (HRR) instantaneously increased by the water mist flow just before rapidly decreasing because the high-speed water mist jet flow pushed the fuel vapor to the side. Some parameters of the water mist spray were carefully selected to get numerical results that are similar to the experiment.

The main goal of the present study is to provide a new and well-documented set of experimental data for the assessment of CFD simulations. More particularly, prior to the fire-water interaction test, a detailed characterization is sought for (1) the water mist spray in the absence of any fire-driven flow, and (2) the fire source in the absence of water. The influence (or not) of the water mist spray on the fire-driven flow is examined experimentally and numerically (using the Fire Dynamics Simulator (FDS), version 6.7.0 [9]) by analyzing (1) the chemical HRR, (2) the gas temperature at the level of the hood (in order to estimate the convective heat flow), and (3) the thermal radiation to the surroundings.

2. Experimental study

A full description of the experimental set-up has been reported in [10]. There are though few differences such the shape of the hood to collect the combustion products and the positions of measurement devices. Only the most important aspects are briefly mentioned here.

2.1 Experimental apparatus and conditions

Figure 1 shows a schematic diagram of the experimental apparatus. The fire source is a propane-gas porous bed burner (diameter 0.15 m). A mass flow meter monitors the mass flow rate of propane gas consumed by the burner. In order to characterize the fire source in the absence of the water mist spray, a thermocouple tree was positioned on the centerline, with 17 thermocouples above the burner surface. Temperatures were recorded for 1200 s, with quasi-steady state time averaged values calculated over a period of 600 s. Radiation corrections were performed [11].

In the exhaust duct, an average volume flow rate of $0.187 \text{ m}^3/\text{s}$ was set before starting the experiment. Four meshes were installed at the sides of the experimental apparatus between the hood and the water collection tank to make the ambient air flow more uniform (Fig. 1). The aperture of the mesh is 0.98 mm and the wire diameter is 0.29 mm , so the aperture ratio is 59.6% .

In the gas analysis system, after extraction and collection of the combustion products, soot and water vapor were removed by a filter and a dehumidifier, and the gas analysis was carried out to measure the concentrations of oxygen, carbon dioxide, and carbon monoxide. Moreover, the mass flow rate of smoke in the duct was determined from measurements of the smoke velocity and temperature in the duct, using a combination of a Pitot tube and a fine differential pressure gauge, and a thermocouple, respectively. One thermos-hygrometer was installed to measure the temperature, T_0 , and humidity, h_0 , of ambient air outside of the experimental apparatus. A second thermos-hygrometer was installed to measure the temperature, T_A , and humidity, h_A , of the gas before the gas analyzers.

Furthermore, the radiative heat flux, q_{rad} , was measured at a horizontal distance of 0.72 m from the fire source and a height of 0.05 m above the burner surface using a 120° -solid angle water-cooled gauge. The temperature, T_h , at the top of the hood was measured by a thermocouple installed at a height of 2.34 m from the surface of the fire source.

In this study, three experiments have been conducted: (1) an experiment to characterize the fire source, (2) an experiment to characterize the water mist spray, and (3) an experiment addressing the interaction between the two. In the latter, ignition occurred 2 minutes after the start of the measurements. After a free-burn period of 11 minutes, the water spray was activated. The interaction between the spray and the fire lasted 5 minutes. Ten minutes later, the supply of propane gas was stopped (referred to hereafter as extinction). The rise in temperature at the top of the hood, ΔT , and the results of the gas analysis were used to estimate the convective heat flow, \dot{Q}_{conv} , and the combustion efficiency, χ , respectively. The convective heat flow was calculated as:

$$\dot{Q}_{conv} = \dot{m}_d c (T_h - T_0) \quad (1)$$

where \dot{m}_d is the mass flow rate in the duct and c is the specific heat of air ($c = 1006 \text{ J}/(\text{kg} \cdot \text{K})$). In the absence of water, Eq. (1) is indicative of the convective heat release rate from the fire. In the presence of a water spray, the convective heat flow is expected to be reduced due to evaporative cooling. In other words, the difference in \dot{Q}_{conv} (before and after the spray) is interpreted as the rate of heat absorbed by water. The combustion efficiency was calculated as:

$$\chi = \frac{\dot{Q}_{ch}}{\dot{Q}_{gas}} \quad (2)$$

where \dot{Q}_{ch} is the chemical HRR calculated by the oxygen consumption method [14] and \dot{Q}_{gas} is the HRR for complete combustion estimated from the mass flow rate of the fuel. The latter two parameters are calculated as:

$$\dot{Q}_{ch} = [(1-f)E' - fE''] X_{O_2}^\circ \phi V_A = [E' - f(E'' - E')] X_{O_2}^\circ \phi V_A \quad (3)$$

$$\dot{Q}_{gas} = \dot{m}_f \Delta H_T \quad (4)$$

where E' is the net heat of combustion per unit volume of oxygen consumed at standard conditions (of 25 °C and 1 atm) and for complete combustion ($E' = 17.2 \text{ MJ/m}^3$), E'' is the net heat of combustion per unit volume of oxygen consumed at standard conditions in the burning of carbon monoxide ($E'' = 23.1 \text{ MJ/m}^3$), X_{O_2} is the volume fraction of oxygen in the ambient air, f is the fraction of depleted oxygen going into the formation of carbon monoxide, ϕ is the fraction of oxygen depleted, V_A is the volume flow rate of air at standard conditions, \dot{m}_f is the mass flow rate of the propane gas, and ΔH_T is the lower calorific value of propane gas ($\Delta H_T = 46.0 \times 10^3 \text{ kJ/kg}$ [15]). The calculation procedure to estimate the uncertainties of the measurements is provided in [10].

2.2 Experimental results

2.2.1 Fire without spray

The measured profiles of \dot{Q}_{conv} , \dot{Q}_{ch} , and \dot{Q}_{gas} (see Eqs. (1), (3), and (4)) are shown in Fig. 3 (left). The average HRR values and the second order standard deviations, determined as the mean values between 1080 and 1680 s under the assumption of quasi-steady combustion, are: $\dot{Q}_{conv} = 12.05 \pm 0.35 \text{ kW}$ ($2\sigma = 2.41$), $\dot{Q}_{ch} = 14.76 \pm 2.73 \text{ kW}$ ($2\sigma = 2.55$), $\dot{Q}_{gas} = 15.43 \pm 0.14 \text{ kW}$ ($2\sigma = 0.02$). This implies a combustion efficiency of about $\chi = 96 \%$.

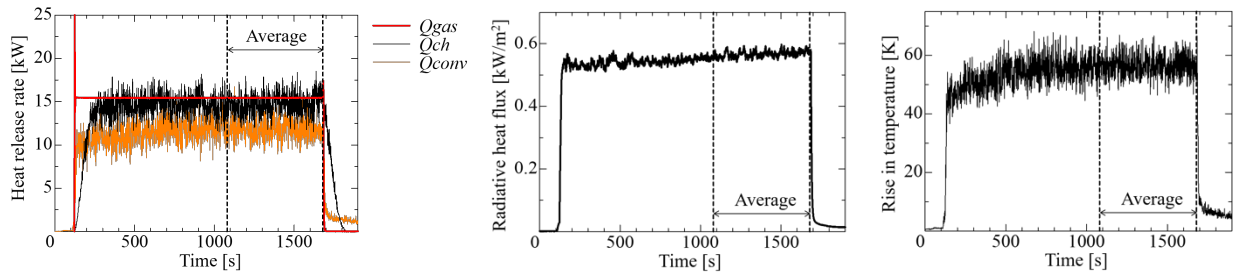


Fig. 3. Evolutions of HRR (left) and radiative heat flux (middle) and temperature rise (right) at the top of the hood over time (no water spray).

The radiative heat flux profile displayed in Fig. 3 (middle) shows a continuous slight rise as the hood and the burner walls gradually heat up. The average values are 0.567 kW/m^2 ($2\sigma = 0.002$) and 56.38 K ($2\sigma = 7.55$), respectively. In Fig. 4, the measured average temperature profile over height on the centerline is shown. The measurements compare well to McCaffrey's correlation [16].

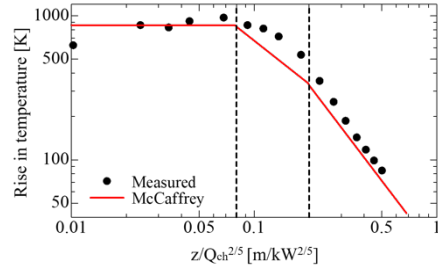


Fig. 4. Evolution of time-averaged measured temperature along the centerline above the burner.

2.2.2 Water spray without fire

Figure 5 shows the measurements for the distribution of the water mass flux at the burner surface. The starting point of axis is the center of the fire source surface and the positive direction of x -axis is along with the direction of the duct. Clearly, there is no perfect circular shape. A spatial integration of the profile displayed in Fig. 5 leads to a water flow rate that is 12% higher than the measured flow rate at the injection. This is indicative of the uncertainty level in the water mass flux distribution measurements.

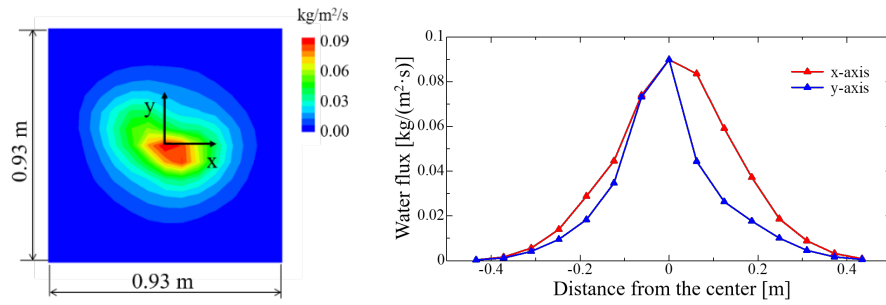


Fig. 5. Water mass flux distribution.

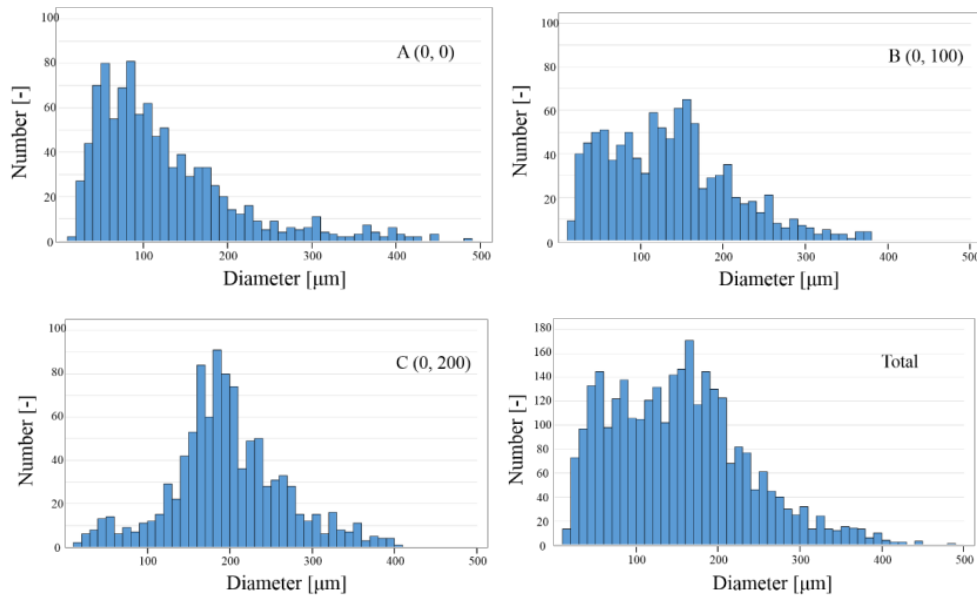


Fig. 6. Droplet size distributions.

Figure 6 shows the droplet size distribution of 1000 droplets at the 3 locations mentioned above, as well as the overall droplet size distribution considering all the droplets collected at the 3 locations.

It can be observed that the further the collection point from the center is, the higher is the droplet diameter at which the peak in the number of droplets occurs. This is expected because the small droplets are ‘easily’ entrained in the core of the spray, whilst the larger ones (with a higher momentum) are able to follow their ‘own’ trajectory. The Sauter mean diameter (SMD) and the volume-median diameter (VMD), $D_{V0.5}$, are reported in Table 1.

Table 1. Mean droplet diameters

(h, r)	A (0, 0)	B (0, 100)	C (0, 200)	Total
SMD [μm]	244.7	209.2	241.7	233.9
$D_{V0.5}$ [μm]	306.8	234.0	253.0	258.2

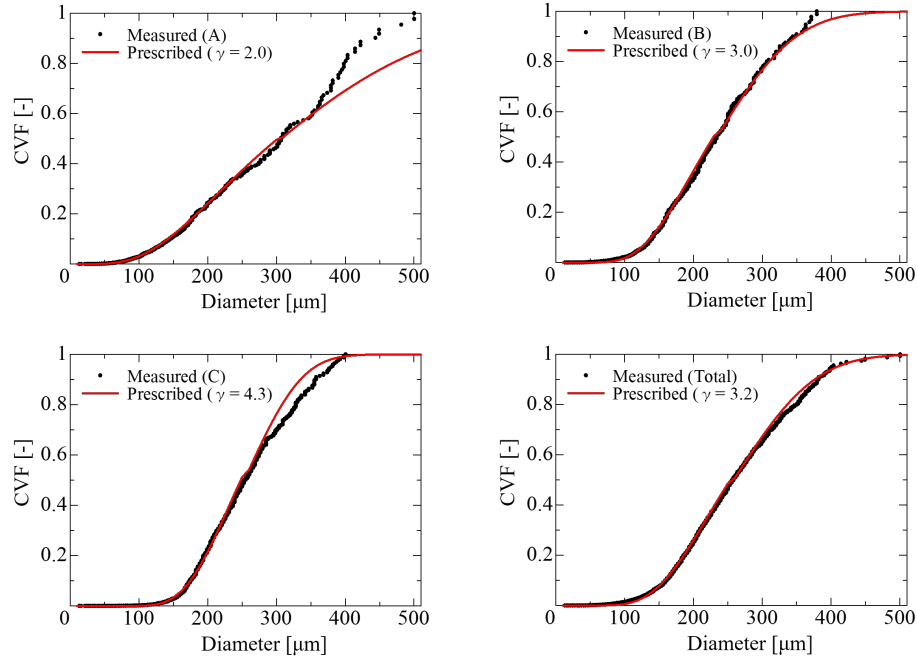


Fig. 7. Comparison of measured droplets size distributions to Eq. (5).

The measured and approximated cumulative volume fraction (CVF) distributions are shown in Fig. 7. The estimated CVF combines log-normal and Rosin-Rammler distributions [17]:

$$F_v(D) = \begin{cases} \frac{1}{\sqrt{2\pi}} \int_0^D \frac{1}{\sigma D'} \exp\left(-\frac{[\ln(D'/D_{v,0.5})]^2}{2\sigma^2}\right) dD' & (D \leq D_{v,0.5}) \\ 1 - \exp\left(-0.693\left(\frac{D}{D_{v,0.5}}\right)^\gamma\right) & (D > D_{v,0.5}) \end{cases} \quad (5)$$

where D is the droplet diameter, γ is the spread factor, and σ is a standard deviation calculated as:

$$\sigma = \frac{2}{\sqrt{2\pi}(\ln 2)\gamma} = \frac{1.15}{\gamma} \quad (6)$$

The measurements follow Eqs. (5) and (6) well, except at position A for diameters larger than 350 μm .

2.2.3 Water spray-flame interaction

Figure 8 shows the measured profiles of \dot{Q}_{conv} , \dot{Q}_{ch} , \dot{Q}_{gas} (from Eqs. (1), (3), and (4)), and $\Delta\dot{Q}_{conv}$ which is the difference of convective heat flow between before and after starting water spraying. In this study, the results are evaluated during three stages: (1) before water spraying (Phase 1), (2) during water spraying (Phase 2), and (3) after water spraying (Phase 3). The time periods considered as steady-state for each stage are: 600–780 s, 900–1080 s, and 1500–1680 s. The average values and the second order standard deviations are reported in Table 2. The convective heat flow decreased by 41.59% between phase 1 and phase 2. As the slight decrease in combustion efficiency during phase 2 is within the uncertainty range, it can be stated that the combustion efficiency is not affected by the water spray. Figure 9, showing the radiative heat flux (left) and temperature rise (right) at the top of the hood, illustrates that q_{rad} , and ΔT decrease by about $28.32 \pm 0.23\%$ and $43.16 \pm 3.16\%$ in Phase 2, but the fire was not suppressed.

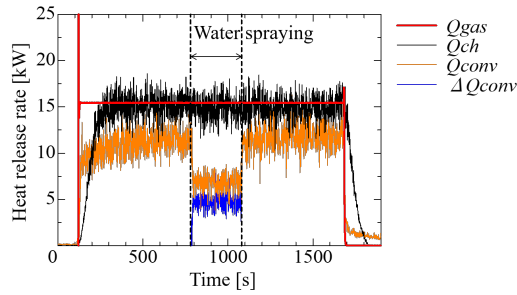


Fig. 8. Evolution of HRR values before, during and after the water spray activation.

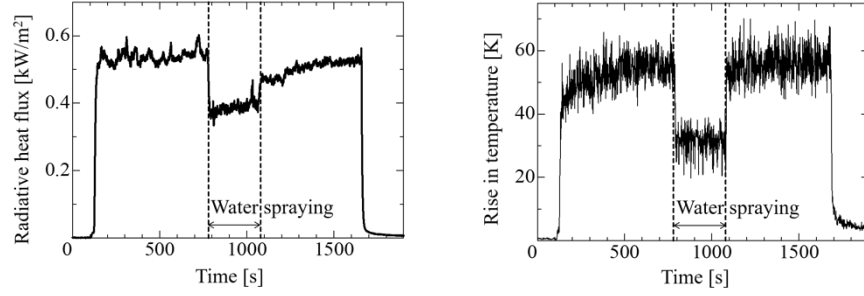


Fig. 9. Experimental results of radiative heat flux (left) and temperature rise (right) at the top of the hood before, during and after the water spray activation.

Table 2. Summary of time-averaged results and the second order standard deviations before (Phase 1), during (Phase 2) and after (Phase 3) activation of the water spray.

	Phase 1		Phase 2		Phase 3	
	Average	2σ	Average	2σ	Average	2σ
χ [%]	98	-	97	-	97	-
\dot{Q}_{gas} [kW]	15.44±0.14	0.03	15.44±0.14	0.03	15.44±0.14	0.03
\dot{Q}_{ch} [kW]	15.07±2.39	2.38	14.96±2.46	2.57	14.94±2.42	2.50
\dot{Q}_{conv} [kW]	11.67±0.38	2.23	6.82±0.35	1.96	12.09±0.39	2.50
$\Delta\dot{Q}_{conv}$ [kW]	-	-	4.85	1.96	-	-
q_{rad} [kW/m²]	0.558±0.001	0.033	0.393±0.001	0.028	0.523±0.000	0.013
ΔT [K]	55.12±1.52	7.46	31.33±1.51	7.16	56.47±1.57	9.15

3. Numerical study

3.1 Computational domain

Figure 10 shows the computational domain and mesh blocks. Unlike in the experimental apparatus, the duct section is a square, rather than circular, but the exhaust velocity was set to $v_{duct} = 3.727$ m/s, yielding the same volume flow rate as in the experiments. The computational domain was divided into 35 blocks, as indicated by the dashed lines in Fig. 10. There is a space of 512 mm (chosen based on the cell size) further from the hood to minimize the effect of the ‘open’ boundary condition on air entrainment. The burner, the hood, the water receiving tank and the duct were modeled as a 1 mm thick stainless steel with an emissivity of 0.34, a density of 7817.0 kg/m³, a conductivity of 16.3 W/(m·K), and a specific heat of 0.46 kJ/(kg·K).

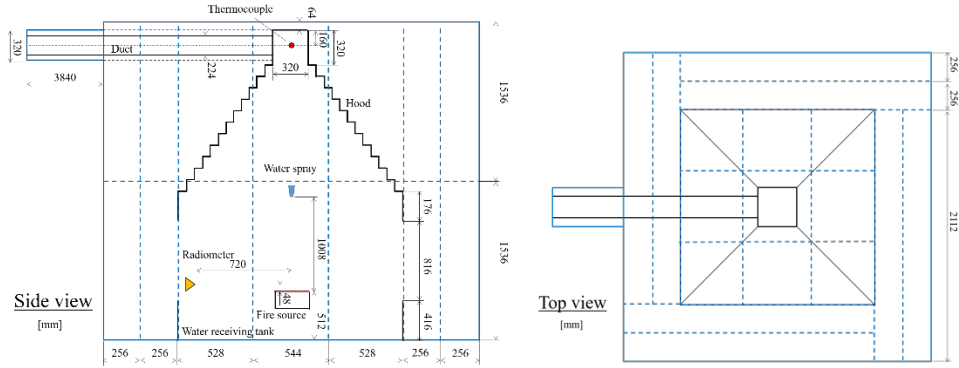


Fig. 10. Computational domain and blocks: side view (left) and top view (right).

3.2 Free burning

The temperature at the top of the hood, the central temperatures of the fire plume, and the radiative heat flux were measured at the same positions of the experimental set-up. The fire source was modeled as a square with a side length of 0.128 m. A heat release rate per unit area of 898.7 kW/m² was prescribed, which corresponds to the HRR of $\dot{Q}_{ch} = 14.8$ kW, as measured in the experiment. Soot and CO yields of respectively 2.4% and 0.5% were prescribed. The default FDS 6.7.0 model settings have been used, e.g., a radiative fraction of 0.3. The simulation time was 60 s and steady-state results were obtained after 30 s. Averaged values have been determined over the last 30 s of the simulations, to compare to the experimentally measured values.

Three cell sizes have been tested: 8 mm, 16 mm, and 32 mm. In the cell sensitivity analysis, the computational domain was reduced by removing the additional space at the sides and thus, reducing the computational times. The temperature distributions along the centerline are shown in Fig. 11 (left). No substantial differences are observed between the 8 mm and the 16 mm simulations. Therefore, the latter was chosen as the cell size for the remainder of the simulations in this study.

It is also important to assess the impact of the number of angles to resolve the radiative heat transfer (which is calculated with the finite volume method in FDS). The default number of angles is 100. A sensitivity analysis has been carried out on this parameter by considering also the values of 400, 800, 1200, 2400, and 3600 on the 16 mm mesh (Fig. 11, right). However, increasing the number of angles leads to an almost linear increase in computational time as well (from about 500 min for 100 angles to about 2000 min for 3600 angles; note that the simulation time has been reduced to 30 s, with averaging over the last 10 s, in order to reduce computing times). Taking this into account, a number of angles of 800 seems a good balance between ‘accuracy’ and computational time. Assuming the radiative heat release rate in case of 800 angles has already reached a steady state, a difference of the heat release rate between 800 angles and 3200 angles was within 5%.

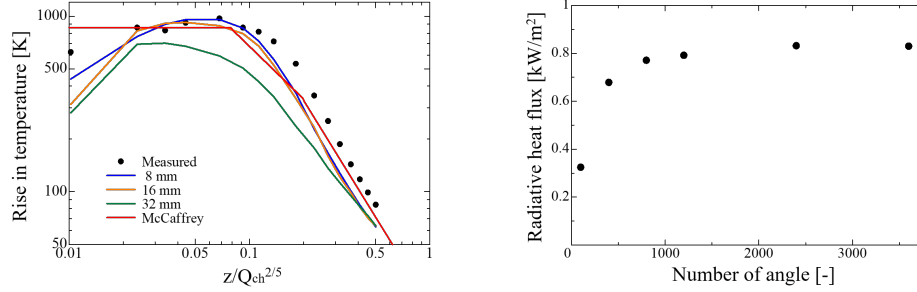


Fig. 11. Mean temperature along the centerline above the burner for different cell sizes (left) and radiative heat flux at the top of the hood for different numbers of angles for radiation (right)

3.3 Water mist spray

For the water mist spray simulations in the absence of fire, the computational domain was reduced to $1600 \times 1600 \times 1664 \text{ mm}^3$ with a passive opening to the outside at all faces. The default FDS 6.7.0 model settings have been used, unless mentioned otherwise. Numerical devices to measure the spray distribution were positioned at the burner height: 15 in the x and y directions, starting from the center and with 64 mm distance between each device. The measurements provided by each device were based on droplets collected within a 32 mm-radius sphere. The spray nozzle was installed at 0.992 m above the measurement points. The settings for the base case are reported in Table 3. The initial velocity was calculated as:

$$v_0 = C \sqrt{\frac{2\Delta P_w}{\rho_d}} \quad (7)$$

where ρ_d is the water density (1000 kg/m^3) and ΔP_w is the operational pressure of the nozzle. The constant C accounts for friction losses in the nozzle, estimated as $C = 0.95$.

Table 3. Base case settings for simulations of the water spray (no fire)

Parameter	Value
Water flow rate [L/min]	0.43
Pressure [MPa]	0.25
Initial velocity [m/s]	21.24
OFFSET [m]	0.032
Orifice diameter [mm]	0.69
Spray angle [°]	56

Figure 12 (left) shows results for the water flux on meshes with a uniform cell size of 8 mm, 16 mm, or 32 mm. The cell sizes of 8 mm and 16 mm yielded very similar results for the spray distribution. A cell size of 16 mm is used for the remainder of the simulations.

It is also important to assess the sensitivity of the results to the number of computational droplets injected per second. Four different values have been tested on the 16 mm mesh: 5000 (which is

the default value in FDS 6.7.0), 50000, and 500000. Figure 12 (right) shows that the numerical profiles were not ‘perfectly’ symmetrical until a value of 50000 droplets per second was used. Thus, the latter value was used for the remainder of the simulations.

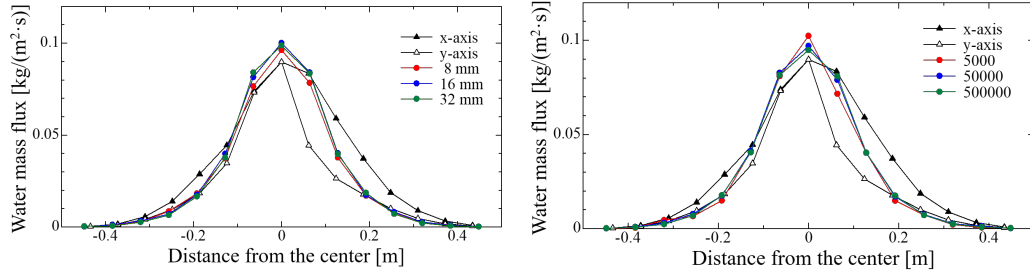


Fig. 12. Water mass flux obtained on different meshes (left) and with different numbers of droplets per second (right).

3.4 Water mist spray-flame interaction

The computational time was set to 90 s, with combustion over the entire period and the water mist spray activated during the last 30 s. The results were averaged half time during each phase (i.e., the last 30 s before activating the water mist spray, and the last 15 s of the simulations).

3.4.1 Heat release rate

The HRR post-processed in FDS [18] is compared to the experimental HRR, \dot{Q}_{ch} , in Fig. 13 (left). The average values in FDS were 14.8 kW in Phase 1 and 14.5 kW in Phase 2. This is in line with the experimental observations in that the HRR is not affected by the water spray.

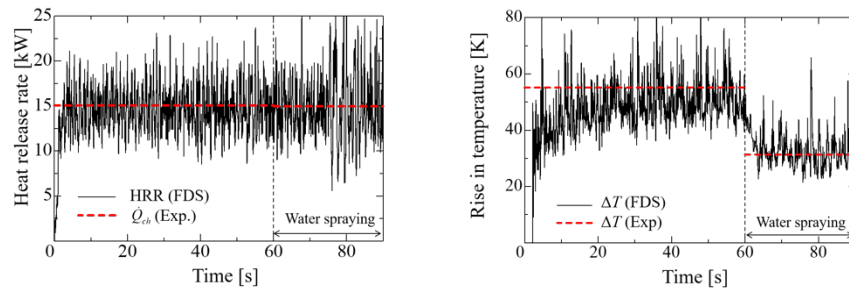


Fig. 13. Comparison CFD results with average of experimental data: HRR (left) and temperature rise at the top of the hood (right).

3.4.2 Temperature rise at the top of the hood

Figure 13 (right) shows the evolution of the temperature rise at the top of the hood. The average value (49.9°C) from the CFD results is somewhat below the experimental value (55.1°C) in Phase 1. This can be partially attributed to inaccuracies in the calculations of the heat losses to

the burner. The agreement in Phase 2 (31.9°C vs 31.3°C) is excellent. The reduction in temperature rise is relatively well captured.

3.4.3 Radiative heat flux

Figure 14 shows the results for the radiative heat flux. In the CFD results, the radiative heat flux does not decrease during the activation of the water spray, in contrast to what is observed experimentally. Actually, the mean value even slightly increases (by about 3 %). Much stronger fluctuations are observed in the radiative heat flux after activation of the water spray.

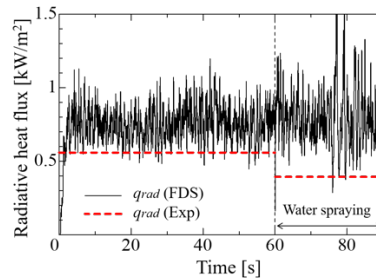


Fig. 14. Comparison CFD results with experimental data: radiative heat flux.

The time-averaged temperature contour plots of phase 1 (before activation of the water spray) and phase 2 (after activation of the water spray) are shown in Fig. 15. The averaging period is 15 s. The irregular patterns in the contour plots indicate that the averaging period is too short, but longer averaging is left for future work. Nevertheless, the contour plots as they are, indicate an overall shortening of the flame under the effect of the water spray, but little effect on the high-temperature region close to the burner. If anything, the region of high temperature (red and orange color) is even a bit larger after activation of the spray. This might explain the slight increase in the predicted radiative heat flux. Another important aspect to mention is that the flame sheet (i.e., the flame surface) cannot be resolved. This is typical for fire simulation and hence a radiative fraction can be defined in FDS, version 6.7.0, such that the overall radiation from the flame is set to a fraction of the total heat release rate. As such, turbulence - radiation interaction is somehow accounted for and the overall radiation is fixed, despite the fact that flame temperatures cannot be calculated accurately on the CFD mesh. To date, we used the same radiative fraction (equal to 0.3) before and after activation of the water spray. This deserves investigation in the future, but can explain why there is so little effect on the radiative heat flux in the simulation results at the moment. Another explanation might be that the influence of water on soot, and its subsequent effect on thermal radiation, is not well accounted for in the modelling. In any case, a more detailed study is required to analyze the absence of ‘radiative shielding’ in the simulations, but this is left for future work. An important factor to bear in mind is that the flame sheet (i.e., the flame surface) is not well-resolved, leading to inaccuracies in the temperature calculations. As a consequence, the radiative fraction is not well-predicted (recall the fourth power dependence on the temperature) and thus, the prescribed radiative fraction of 0.3 continues to be used during water spraying. Another explanation would be that the influence of water on soot and its subsequent thermal radiation is not well accounted for in the modelling. A more detailed study is required to analyze the absence of ‘radiative shielding’ in the simulations.

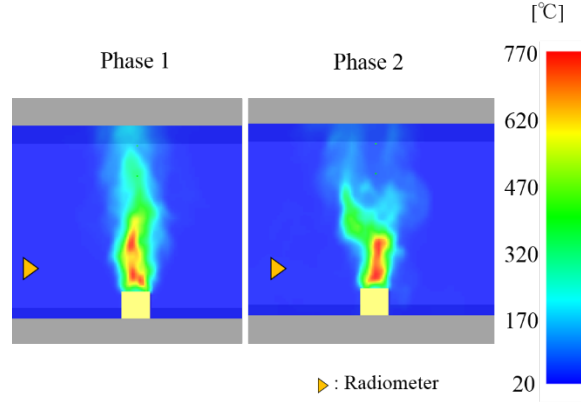


Fig. 15. Time-averaged contour plots of temperature distribution over 15 s.

3.4.4 Heat absorbed by the droplets

In FDS, the heat absorbed per unit time by the droplets, \dot{Q}_{part} , is post-processed as an output [18]. The obtained value is $\dot{Q}_{part} = 3.68$ kW. This value is relatively in good agreement with the reduction in the convective heat flow, $\Delta\dot{Q}_{conv} = 3.20$ kW (see Fig. 16). This is quite interesting knowing that the former stems from an integration of local values over the whole domain and for all the droplets, whereas the latter is estimated from a local measurement of the gas temperature and mass flow rate near the exhaust duct. Furthermore, the slightly higher value (by 15 %) of the heat absorbed by the droplets might be attributed to thermal radiation attenuation by the droplets (in addition to smoke cooling that is associated to the convective heat flow). These aspects will be further analyzed and can contribute to a more detailed assessment of heat transfer around droplets in fire-driven flows. The predicted reduction in the convective heat flow is underpredicted by 34 % (the experimental value is $\Delta\dot{Q}_{conv} = 4.85$ kW), despite the good agreement in the temperature at the water spraying stage, see Fig. 16. The deviation is attributed to the underprediction in the gas temperature prior to water activation, see Fig. 16.

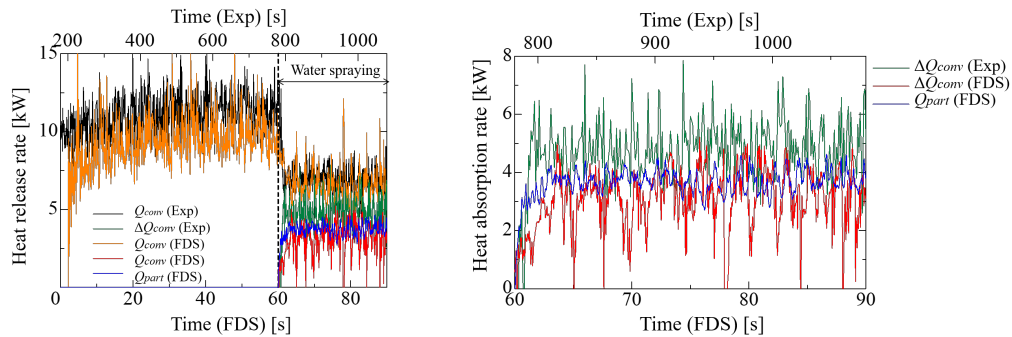


Fig. 16. Computational result of the heat absorption rate.

4. Conclusion

The goal of this study is to assess the current CFD capabilities for the prediction of the interaction between a water mist spray and a turbulent buoyant flame.

First, three experiments were conducted: (1) an experiment to characterize the fire source (heat release rate, combustion efficiency, thermal radiation to the surrounding, temperature profile in the centerline), (2) an experiment to characterize the water spray (droplet size distribution and water mass flux distribution), and (3) an experiment addressing the interaction between the two (reduced convective heat flow rate, thermal radiation, and heat absorbing by droplets). As a result, the temperature at the top of the hood and the radiative heat flux decreased about 40% and 30%, respectively, while the rate of chemical heating did not change during the activation of the water mist spray. It is important to recall that this outcome is not representative of all the possible expected effects of mist systems, e.g., flame cooling. Nevertheless, the obtained dataset is very useful for the assessment of the current CFD capabilities.

Second, a CFD study of the interaction between the fire and the water spray has been undertaken with, first, a separate numerical characterization of the fire source and the water mist spray. A sensitivity analysis for the free-burning flame simulation has shown that a cell size of 16 mm and a number of solid angles of 800 were ‘appropriate’ for the case at hand. For the water mist spray simulation, a cell size of 16 mm is also shown to be ‘appropriate’, in addition to a number of 500000 droplets per second.

Similarly to the experiments, the CFD study shows that the heat release rate remains constant during the activation of the water mist spray. A relatively good agreement was also obtained for the gas temperature at the extraction duct during water spray activation. An underprediction of the temperature prior to water spray activation resulted in an underprediction of the overall convective heat flow reduction. Furthermore, it has been shown that the heat absorption rate by the fine droplets can be estimated from the convective heat flow rate, which is based on the temperature and the mass flow rate of gas near the hood.

However, as opposed to the experiments, the predicted radiative heat flux did not decrease during water spray activation. This is primarily attributed to the fact that the radiative fraction is not well-resolved because the temperature near the flame surface cannot be calculated exactly on the coarse numerical grid. Nevertheless, further analysis is required to explain the discrepancy with the experimental result.

5. Acknowledgements

This work was supported by Japan Student Services Organization, Japan Public-Private Partnership Student Study Abroad Program (TOBITATE! Young Ambassador Program).

6. References

- [1] H.M. Iqbal Mahmudn, Khalid A. M. Moinuddin, Graham R. Thorpe, Experimental and numerical study of high-pressure water-mist nozzle sprays, *Fire Saf. J.* 81 (2016) 109–117.

- [2] Xiangyang Zhou, Stephen P. D’Aniello, Hong-Zeng Yu, Spray characterization measurements of a pendent fire sprinkler, *Fire Saf. J.* 54 (2012) 36–48.
- [3] Xiangyang Zhou, Characterization of interactions between hot air plumes and water sprays for sprinkler protection, *Proc. Combust. Inst.* 35 (2015) 2723–2729.
- [4] Yang Zhou, Rongwei Bu, Xiaonan Zhang, Chuangang Fan, Junhui Gong, Performance evaluation of water mist fire suppression: A clean and sustainable fire-fighting technique in mechanically-ventilated place, *Journal of Cleaner Production* 209 (2019) 1319–1331.
- [5] Paolo E. Santangelo, Bryson C. Jacobs, Ning Ren, Joshua A. Sheffel, May L. Corn, André W. Marshall, Suppression effectiveness of water-mist sprays on accelerated wood-cribfires, *Fire Saf. J.* 70 (2014) 98–111.
- [6] T. Beji, G. Maragkos, S.E. Zadeh, B. Merci, Numerical modelling of the interaction between water sprays and hot air jets—part i: gas phase large eddy simulations, *Fire Saf. J.* 95 (2018) 77–86.
- [7] T. Beji, S.E. Zadeh, G. Maragkos, B. Merci, Numerical modelling of the interaction between water sprays and hot air jets—part ii: Two-phase flow simulations, *Fire Saf. J.* 96 (2018) 143–152.
- [8] Jaiho Lee, Numerical analysis on the rapid fire suppression using a water mist nozzle in a fire compartment with a door opening, *Nuclear Engineering and Technology* 51 (2019) 410–423.
- [9] Kevin McGrattan, Simo Hostikka, Randall McDermott, Jason Floyd, Marcos Vanella, *Fire Dynamics Simulator User’s Guide*, NIST Special Publication 1019 Sixth Edition
- [10] F. Tanaka, W. Mizukami, Khalid A. M. Moinuddin, Fire cooling performance by water sprays using medium and small-scale model experiments with scaling relation, *Fire Saf. J.* (in review)
- [11] L.G. Blevins, W.M. Pitts, Modeling of bare and aspirated thermocouples in compartment fires, *Fire Safety Journal* 33 (1999) 239–259
- [12] E.T. Hurlburt, T.J. Hanratty, Measurement of drop size in horizontal annular flow with the immersion method, *Experiments in Fluids* 32 (2002) 692–699.
- [13] T. Fujimatsu, M. Kito, and K. Kondo, Droplet size measurement of liquid atomization by the immersion liquid method (droplet coalescence and solution into the immersion liquid), *Advances in Fluid Mechanics X (The proceedings of the tenth International Conference on Advances in Fluid Mechanics)*, WIT Transactions on Engineering Sciences 82, WIT Press, (2014), 191–202.
- [14] W.J. Parker, Calculations of the heat release rate by oxygen consumption for various applications, NBSIR 81-2427-1, National Bureau of Standards (U.S.), March 1982.
- [15] M.J. Hurley, (Ed.), *SFPE Handbook of Fire Protection Engineering* (fifth edition), Society of Fire Protection Engineers (2016).
- [16] McCaffrey B. J, Purely buoyant diffusion flames: some experimental results, NBSIR79-1910 (1979).
- [17] T.S. Chen, Measurements of water density and droplet size distributions of selected ESFR sprinklers, *Journal of Fire Protection Engineering*, 6(2) (1994) 79–87.
- [18] Kevin McGrattan, Simo Hostikka, Randall McDermott, Jason Floyd, Marcos Vanella, *Fire Dynamics Simulator User’s Guide*, NIST Special Publication 1019 Sixth Edition, 260 p.

Figure captions

Fig. 1. Experimental apparatus, showing the fire source, water spray system, exhaust system and gas analysis system.

Fig. 2. Photo of spray angle (left) and schematic diagram of the positioning of the cups to measure the water flow rate distribution at the burner surface (right).

Fig. 3. Evolutions of HRR (left) and radiative heat flux (middle) and temperature rise (right) at the top of the hood over time (no water spray).

Fig. 4. Evolution of time-averaged measured temperature along the centerline above the burner.

Fig. 5. Water mass flux distribution.

Fig. 6. Droplet size distributions.

Fig. 7. Comparison of measured droplets size distributions to Eq. (5).

Fig. 8. Evolution of HRR values before, during and after the water spray activation.

Fig. 9. Experimental results of radiative heat flux (left) and temperature rise (right) at the top of the hood before, during and after the water spray activation.

Fig. 10. Computational domain and blocks: side view (left) and top view (right).

Fig. 11. Mean temperature along the centerline above the burner for different cell sizes (left) and radiative heat flux at the top of the hood for different numbers of angles for radiation (right)

Fig. 12. Water mass flux obtained on different meshes (left) and with different numbers of droplets per second (right).

Fig. 13. Comparison CFD results with average of experimental data: HRR (left) and temperature rise at the top of the hood (right).

Fig. 14. Comparison CFD results with experimental data: radiative heat flux.

Fig. 15. Time-averaged contour plots of temperature distribution over 15 s.

Fig. 16. Computational result of the heat absorption rate.

A. Estimation of the uncertainties in the Heat Release Rate (HRR) calculations

In this experiments, the measurement uncertainties of Q_{conv} , Q_{ch} , and Q_{gas} were calculated as:

$$U = \left(B^2 \pm (tS_{\bar{x}})^2 \right)^{1/2} \quad (19)$$

U is Measurement uncertainty at a 95% confidence level, B is the bias limit, Student's t value is the estimate value of the precision error limit and evaluated as two because the data measured at 1-s intervals and evaluated the value averaged for 180 seconds, and $S_{\bar{x}}$ is the precision index of average. Q_{conv} , and Q_{ch} were calculated using many parameters measured as follow.

$$Q_{conv} = func(T_d, \Delta P, T_h, T_0) \quad (20)$$

$$Q_{ch} = func(X_{O_2}, X_{CO_2}, X_{CO}, T_d, \Delta P, T_A, h_A, T_0, h_0) \quad (21)$$

These parameters have the bias limit and the precision index of average, respectively. Therefore, the bias limit and the precision index of average were estimated as follows:

$$B_{Q_{conv}} = \left\{ \left(\theta_{T_d} B_{T_d} \right)^2 + \left(\theta_{\Delta P} B_{\Delta P} \right)^2 + \left(\theta_{T_h} B_{T_h} \right)^2 + \left(\theta_{T_0} B_{T_0} \right)^2 \right\}^{1/2} \quad (22)$$

$$B_{Q_{ch}} = \left\{ \left(\theta_{X_{O_2}} B_{X_{O_2}} \right)^2 + \left(\theta_{X_{CO_2}} B_{X_{CO_2}} \right)^2 + \left(\theta_{X_{CO}} B_{X_{CO}} \right)^2 + \left(\theta_{T_d} B_{T_d} \right)^2 + \left(\theta_{\Delta P} B_{\Delta P} \right)^2 + \left(\theta_{T_A} B_{T_A} \right)^2 + \left(\theta_{h_A} B_{h_A} \right)^2 + \left(\theta_{T_0} B_{T_0} \right)^2 + \left(\theta_{h_0} B_{h_0} \right)^2 \right\}^{1/2} \quad (23)$$

$$S_{\bar{x}_{Q_{conv}}} = \left\{ \left(\theta_{T_d} S_{\bar{x}_{T_d}} \right)^2 + \left(\theta_{\Delta P} S_{\bar{x}_{\Delta P}} \right)^2 + \left(\theta_{T_h} S_{\bar{x}_{T_h}} \right)^2 + \left(\theta_{T_0} S_{\bar{x}_{T_0}} \right)^2 \right\}^{1/2} \quad (24)$$

$$S_{\bar{x}_{Q_{ch}}} = \left\{ \left(\theta_{X_{O_2}} S_{\bar{x}_{X_{O_2}}} \right)^2 + \left(\theta_{X_{CO_2}} S_{\bar{x}_{X_{CO_2}}} \right)^2 + \left(\theta_{X_{CO}} S_{\bar{x}_{X_{CO}}} \right)^2 + \left(\theta_{T_d} S_{\bar{x}_{T_d}} \right)^2 + \left(\theta_{\Delta P} S_{\bar{x}_{\Delta P}} \right)^2 + \left(\theta_{T_A} S_{\bar{x}_{T_A}} \right)^2 + \left(\theta_{h_A} S_{\bar{x}_{h_A}} \right)^2 + \left(\theta_{T_0} S_{\bar{x}_{T_0}} \right)^2 + \left(\theta_{h_0} S_{\bar{x}_{h_0}} \right)^2 \right\}^{1/2} \quad (25)$$

Table 2 lists the bias limits for all the instruments, the precision indexes of average for all the measurement values, and sensitivity for all measurement values.

Table 4 List of all the bias limits and the precision index of average

	Parameter i	Description	Units	B_i	$S_{\bar{x}_i}$	θ_i
\dot{Q}_{conv}	ΔP	Pressure difference in the duct	Pa	2.5×10^{-1}	7.2×10^{-2}	7.1×10^{-1}
	T_d	Temperature in the duct	K	1.0	7.2×10^{-2}	1.8×10^{-2}
	T_d	Temperature in the duct	K	1.0	7.2×10^{-2}	5.8×10^{-1}
	T_h	Temperature in the top of the hood	K	1.0	1.5×10^{-1}	2.1×10^{-1}
	T_0	Ambient temperature	K	1.5×10^{-1}	2.5×10^{-3}	2.1×10^{-1}
\dot{Q}_{ch}	X_{O_2}	O ₂ volume fraction	-	1.7×10^{-6}	1.7×10^{-4}	3.8×10^{-3}
	X_{CO_2}	CO ₂ volume fraction	-	1.1×10^{-6}	2.4×10^{-6}	7.8×10^{-6}
	X_{CO}	CO volume fraction	-	1.1×10^{-8}	2.3×10^{-8}	1.3×10^{-11}

T_d	Temperature in the duct	K	1.0	7.2×10^{-2}	2.2×10^{-2}
ΔP	Pressure difference in the duct	Pa	2.5×10^{-1}	7.2×10^{-2}	7.1×10^{-1}
T_A	Temperature in the analyzer	K	1.5×10^{-1}	3.1×10^{-3}	1.4×10^{-5}
h_A	Humidity in the analyzer	%	2.0×10^{-2}	1.7×10^{-15}	4.4×10^{-3}
T_0	Ambient temperature	K	1.5×10^{-1}	2.4×10^{-3}	1.6×10^{-4}
h_0	Ambient humidity	%	2.0×10^{-2}	2.0×10^{-2}	3.9×10^{-3}

513

514